

# The $\nu^2$ GC Simulations : Quantifying the Dark Side of the Universe in the Planck Cosmology

Tomoaki ISHIYAMA<sup>1,2</sup>

<sup>1</sup>*Institute of Management and Information Technologies, Chiba University, 1-33, Yayoi-cho, Inage-ku, Chiba, 263-8522, Japan*

<sup>2</sup>*Center for Computational Science, University of Tsukuba, 1-1-1, Tennodai, Tsukuba, Ibaraki, 305-8577, Japan*  
 ishiyama@chiba-u.jp

Motohiro ENOKI<sup>3</sup>

<sup>3</sup>*Faculty of Business Administration, Tokyo Keizai University, Kokubunji, Tokyo, 185-8502, Japan*  
 Masakazu A.R. KOBAYASHI<sup>4</sup>

<sup>4</sup>*Research Center for Space and Cosmic Evolution, Ehime University, Matsuyama, Ehime, 790-8577, Japan*  
 Ryu MAKIYA<sup>5</sup>

<sup>5</sup>*Institute of Astronomy, the University of Tokyo, Mitaka, Tokyo, 181-0015, Japan*  
 Masahiro NAGASHIMA<sup>6,7</sup>

Taira OOGI<sup>6,7</sup>

<sup>6</sup>*Faculty of Education, Nagasaki University, Nagasaki, Nagasaki, 852-8521, Japan*

<sup>7</sup>*Faculty of Education, Bunkyo University, Koshigaya, Saitama 343-8511, Japan*

(Received ( ); accepted ( ))

## Abstract

We present the evolution of dark matter halos in six large cosmological  $N$ -body simulations, called the  $\nu^2$ GC (New Numerical Galaxy Catalog) simulations on the basis of the  $\Lambda$ CDM cosmology consistent with observational results obtained by the Planck satellite. The largest simulation consists of  $8192^3$  (550 billion) dark matter particles in a box of  $1.12 h^{-1}\text{Gpc}$  (a mass resolution of  $2.20 \times 10^8 h^{-1}M_\odot$ ). Among simulations utilizing boxes larger than  $1 h^{-1}\text{Gpc}$ , our simulation yields the highest resolution simulation that has ever been achieved. A  $\nu^2$ GC simulation with the smallest box consists of eight billions particles in a box of  $70 h^{-1}\text{Mpc}$  (a mass resolution of  $3.44 \times 10^6 h^{-1}M_\odot$ ). These simulations can follow the evolution of halos over masses of eight orders of magnitude, from small dwarf galaxies to massive clusters. Using the unprecedentedly high resolution and powerful statistics of the  $\nu^2$ GC simulations, we provide statistical results of the halo mass function, mass accretion rate, formation redshift, and merger statistics, and present accurate fitting functions for the Planck cosmology. By combining the  $\nu^2$ GC simulations with our new semi-analytic galaxy formation model, we are able to prepare mock catalogs of galaxies and active galactic nuclei, which will be made publicly available in the near future.

**Key words:** cosmology: theory —methods: numerical —galaxies: structure —galaxies: formation —dark matter

## 1. Introduction

Galaxy formation is one of the fundamental processes driving the evolution of our Universe. However, the details of its underlying mechanisms are not well understood. There are many physical processes involved in galaxy formation and evolution such as star formation, active galactic nuclei (AGN) formation, their feedback, and supernovae. For example, observations have demonstrated that masses of supermassive blackholes in galactic centers correlate with the stellar masses and stellar velocity dispersions of galactic bulges (e.g., Magorrian et al. 1998). This correlation suggests that galaxies and supermassive blackholes in galactic centers co-evolve while interacting with each other. However, the details of the physical processes involved in their interactions are not well understood.

Some cosmological hydrodynamic simulations for galaxy and AGN formation have partially succeeded in reproducing observational results such as the AGN lu-

minosity function and AGN number density evolution (e.g., Degraf et al. 2010; Hirschmann et al. 2014; Khandai et al. 2014). However, sufficient data to demonstrate the result's statistical significance are lacking. To improve the mass resolution of these simulations, relatively small simulation boxes have been used (less than  $100 h^{-1}\text{Mpc}$ ), making it difficult to follow the formation and evolution of numerous galaxies and AGNs at high redshifts. Since cosmological hydrodynamic simulations with large boxes and sufficient mass resolution remain computationally challenging, a large gap exists between numerical simulations and observations for high redshifts.

One way to bridge this gap is to use a semi-analytic galaxy formation model in which galaxy and AGN formation is modeled phenomenologically within merger histories of dark matter halos (merger trees) taken from cosmological  $N$ -body simulations or the analytic extended Press–Schechter model (EPS; Peacock & Heavens 1990; Bond et al. 1991; Bower 1991). Examples of success-

ful semi-analytic galaxy formation models are the  $\nu$ GC (Nagashima et al. 2005) model based on the Mitaka model (Nagashima & Yoshii 2004) and its successor, the  $\nu^2$ GC model (Makiya et al., in prep). Most recent semi-analytic models use merger trees taken from large cosmological  $N$ -body simulations, which can easily provide spatial information about galaxies and AGNs. Generating merger trees using the EPS method is appealing because the computational cost is low. However, this method does not provide spatial information, and its merger statistics are significantly different from those of cosmological simulations (e.g., Jiang & van den Bosch 2014).

The rarity of the objects that can be obtained in semi-analytic models depends on the box size of the adopted cosmological  $N$ -body simulations. In particular, bright AGNs at high redshifts are rare objects. Their number density is only  $\sim 10^{-8}$ – $10^{-6} \text{ Mpc}^{-3} \text{ mag}^{-1}$  (e.g., Fontanot et al. 2007; Croom et al. 2009; Ikeda et al. 2011; Ikeda et al. 2012). To obtain a statistically significant number of mock galaxies and AGNs at high redshifts, a high mass resolution and large spatial volume are necessary. Our previous study, which was based on a cosmological simulation with  $2048^3$  particles in a  $280 h^{-1} \text{ Mpc}$  box, shows that the AGN downsizing trend naturally emerges (Enoki et al. 2014). However, the number of AGNs at  $z = 2$  was only  $\sim 10^{-6} \text{ Mpc}^{-3} \text{ mag}^{-1}$ , complicating the discussion of the spatial clustering of AGNs and their evolution. Galaxies at high redshifts are smaller than those at low redshifts. A high mass resolution is required to follow the hierarchical formation of these small galaxies. To compare these results with forthcoming wide and deep observations of galaxies and AGNs provided by the Subaru Hyper-Suprime-Cam (Miyazaki et al. 2006; Miyazaki et al. 2012), we need extremely large simulations based on state-of-the-art cosmology.

Most of the simulations in the existing literature do not meet these requirements. One typical simulation suite that succeeded in many scientific aspects is the Millennium runs (Springel et al. 2005; Boylan-Kolchin et al. 2009; Angulo et al. 2012). The box sizes of the Millennium and Millennium-XXL simulations are  $500 h^{-1} \text{ Mpc}$  and  $3 h^{-1} \text{ Gpc}$ , respectively, which are large enough to obtain a large number of bright AGNs. However, their mass resolutions are too poor to capture small galaxy formations. The box size of the Millennium-II simulation ( $100 h^{-1} \text{ Mpc}$ ) is too small to obtain a sufficient number of AGNs, but its mass resolution is better than the other Millennium variations. Thus, it may be difficult to compare mock catalogs of these simulations with forthcoming wide and deep AGN observations. The cosmology of the Millennium runs is based on the first year Wilkinson microwave anisotropy probe (WMAP) data (Spergel et al. 2003), which differs significantly from recent results obtained by the Planck satellite (Planck Collaboration et al. 2014). However, the different cosmology may not be a problem by using a rescaling algorithm (Angulo & White 2010; Angulo & Hilbert 2014), as also shown in Guo et al. (2013) and Henriques et al. (2014).

To address these problems, we conducted a suite of ultralarge cosmological  $N$ -body simulations, the  $\nu^2$ GC simulation suite. The largest volume used in this suite is  $1.12 h^{-1} \text{ Gpc}$ , and the highest mass resolution is  $3.44 \times 10^6 h^{-1} M_\odot$ . The largest  $\nu^2$ GC simulation includes  $8192^3 = 549,755,813,888$  dark matter particles in a box of  $1.12 h^{-1} \text{ Gpc}$ . The mass of each particle is  $2.20 \times 10^8 h^{-1} M_\odot$ . Compared with the Millennium simulation (Springel et al. 2005), our simulation offers the advantages of a mass resolution that is four times better and a spatial volume that is 11 times larger. Simulations utilizing boxes greater than  $1 h^{-1} \text{ Gpc}$  have previously achieved mass resolutions peaking at an order  $10^9 h^{-1} M_\odot$  (Teyssier et al. 2009; Angulo et al. 2012; Skillman et al. 2014). Our mass resolution is more than 20 times higher than other large volume simulations. The cosmology of our simulation is based on state-of-the-art observational results obtained by the Planck satellite (Planck Collaboration et al. 2014), which provide significantly different cosmological parameters from those adopted in previous studies. By accomplishing unprecedentedly high mass resolution and statistical power, our simulation is more advanced than any simulation to date and provides the most accurate tools for studying galaxy and AGN formation and cosmology.

In this study, we present details of the  $\nu^2$ GC simulations. In §2, we describe the basic properties of the simulations and the applied numerical methods. The basic results, including mass function, mass accretion rate, statistics of formation redshift, and statistics of merger, are presented in §3. The results are summarized in §4. The details of our  $\nu^2$ GC semi-analytic model are also presented in a companion study (Makiya et al., in prep).

## 2. The $\nu^2$ GC Simulation Suite

### 2.1. Simulation Details

The  $\nu^2$ GC simulation suite consists of six large cosmological  $N$ -body simulations with varying mass resolutions and box sizes. The details of the six simulations are outlined in Table 1. In the largest run, named  $\nu^2$ GC-L, we simulated the motions of  $8192^3 = 549,755,813,888$  dark matter particles with a mass resolution of  $2.20 \times 10^8 h^{-1} M_\odot$  in a comoving box of  $1120 h^{-1} \text{ Mpc}$ . We performed two simulations with smaller boxes and the same mass resolution, namely,  $4096^3$  particles in a  $560 h^{-1} \text{ Mpc}$  box ( $\nu^2$ GC-M) and  $2048^3$  particles in a  $280 h^{-1} \text{ Mpc}$  box ( $\nu^2$ GC-S). These smaller simulations allow us to perform resolution studies. In two additional runs, we simulated the motions of  $2048^3$  particles using higher mass resolutions and smaller boxes than those of the other three simulations. We named these simulations  $\nu^2$ GC-H1 and  $\nu^2$ GC-H2. The box size and mass resolution of the former are  $140 h^{-1} \text{ Mpc}$  and  $2.75 \times 10^7 h^{-1} M_\odot$ , and those of the latter are  $70 h^{-1} \text{ Mpc}$  and  $3.44 \times 10^6 h^{-1} M_\odot$ . These five simulations were terminated at  $z = 0$ . In the final simulation, named  $\nu^2$ GC-H3, we simulated  $4096^3$  particles in a  $140 h^{-1} \text{ Mpc}$  box down to  $z = 4$ . Since this simulation adopts an equivalent mass resolution and eight times

larger spatial volume compared with those of  $\nu^2$ GC-H2, galaxies may be studied at high redshifts with unprecedentedly high mass resolutions and statistics.

The initial conditions used in these simulations were generated by a publicly available code, 2LPTic<sup>1</sup>, using second-order Lagrangian perturbation theory (e.g., Crocce et al. 2006). The adopted cosmological parameters were based on an observation of the cosmic microwave background obtained by the Planck satellite (Planck Collaboration et al. 2014), namely,  $\Omega_0 = 0.31$ ,  $\Omega_b = 0.048$ ,  $\lambda_0 = 0.69$ ,  $h = 0.68$ ,  $n_s = 0.96$ , and  $\sigma_8 = 0.83$ . To calculate the transfer function, we used the online version<sup>2</sup> of CAMB (Lewis et al. 2000). All simulations began at  $z = 127$ .

Simulations were performed by GreeM<sup>3</sup> (Ishiyama et al. 2009a; Ishiyama et al. 2012), a massively parallel TreePM code, on the K computer at the RIKEN Advanced Institute for Computational Science, and Aterui super-computer at Center for Computational Astrophysics, CfCA, of National Astronomical Observatory of Japan. To accelerate the calculation of the tree force, we used the Phantom-GRAPE library<sup>4</sup> (Nitadori et al. 2006; Tanikawa et al. 2012; Tanikawa et al. 2013) with support for the HPC-ACE architecture of the K computer and AVX instruction set extension to the x86 architecture.

For the largest  $\nu^2$ GC-L simulation, we used 16,384 nodes of the K computer. Each node consists of one SPARC64 VIIIfx oct-core processor with the clock speed of 2.0 GHz and 16 GB memory. We performed the simulation with 16,384 MPI tasks, in which eight OpenMP threads ran in parallel. The calculation time was 50 ~ 60 seconds per step with global and adaptive timesteps. The total CPU time and memory consumed were 11 million CPU hours (1.38 million node hours) and about 50TB. At  $z = 0$ , the maximum CPU and memory imbalances are about 3% and 25%. The relatively large imbalance of memory consumption ensured nearly ideal load balance.

The dataset of the particles was stored at 51 time slices from  $z = 20$  to  $z = 0$  for the  $\nu^2$ GC-L,  $\nu^2$ GC-M, and  $\nu^2$ GC-S simulations. From  $z = 7.54$ , total 46 output redshifts were selected, as the time interval is proportional to the typical dynamical time of the halos. The corresponding logarithmic redshift interval  $\Delta \log(1+z)$  is 0.02–0.03. Moreover, six datasets at high redshifts of  $z = 8.15$ , 10.0, 12.9, 16.2, and 20.0 were stored. For the  $\nu^2$ GC-H1 and  $\nu^2$ GC-H2 simulations, the 46 output redshifts from  $z = 7.54$  were identical to those of the first three simulations. Furthermore, from  $z = 12.5$  to  $z = 7.54$ , 10 datasets with a constant logarithmic redshift interval of  $\Delta \log(1+z) = 0.02$  and two datasets at high redshifts of  $z = 16.2$ , 20.0 were stored. Thus there are total 58 time slices for the  $\nu^2$ GC-H1 and  $\nu^2$ GC-H2 simulations. For the  $\nu^2$ GC-H3 simulation, the output redshifts were identical to those of the  $\nu^2$ GC-H1

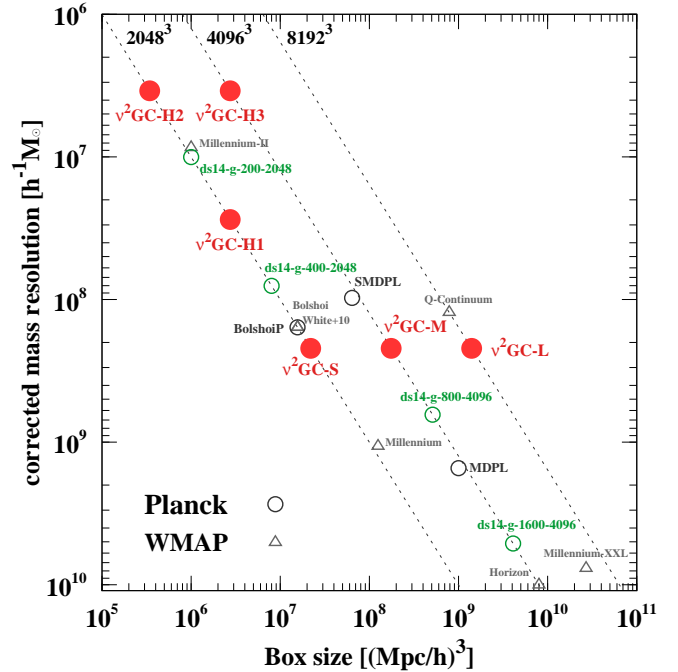


**Fig. 1.** Mass resolution versus simulation volume of recent large cosmological  $N$ -body simulations. The mass resolution of each simulation is corrected as the cosmological parameters of all simulations are the same as those we chose. The number of particles along the three dashed lines is constant. Circles show simulations based on the Planck cosmology. The six red filled circles are the  $\nu^2$ GC simulations. The four green circles denote four of the five Dark Sky Simulations (DSS; Skillman et al. 2014). The mass resolution of the rest of the DSS simulations is below the range of this figure. The three black circles are the BolshoiP, MDPL and SMDPL simulations (Klypin et al. 2014). Gray open triangles show simulations based on the WMAP cosmology by other groups, Millennium simulation (Springel et al. 2005), Horizon (Teyssier et al. 2009), Millennium-II (Boylan-Kolchin et al. 2009), White+10 (White et al. 2010), Bolshoi (Klypin et al. 2011), Millennium-XXL (Angulo et al. 2012), and Q Continuum (Heitmann et al. 2014).

and  $\nu^2$ GC-H2 simulations, and 22 datasets were stored down to  $z = 4$ .

We compare the effectiveness of the  $\nu^2$ GC simulations with that of the other recent large cosmological simulations in Figure 1. The figure includes simulations with particle mass resolutions better than  $10^{10} h^{-1} M_\odot$ , box sizes larger than  $70 h^{-1} \text{Mpc}$ , and particle numbers larger than  $2048^3$ . To resolve the effective Jeans mass at high redshifts, the critical mass resolution of halos is  $\sim 10^9$ – $10^{10} h^{-1} M_\odot$  (Nagashima et al. 2005). Thus, only our  $\nu^2$ GC-L and  $\nu^2$ GC-M simulations are able to accurately follow the physical processes of the formation and evolution of galaxies and bright AGNs in the context of the hierarchical structure formation scenario based on the concordance cosmology. Clearly, there is a severe lack of large simulations for small galaxies based on the Planck cosmology, which our  $\nu^2$ GC simulations fill. Just before the completion of this study, a simulation with volume and

<sup>1</sup> <http://cosmo.nyu.edu/roman/2LPT/>

We slightly modified the code to enable a more rapid generation of initial conditions with over  $2048^3$  particles.

<sup>2</sup> [http://lambda.gsfc.nasa.gov/toolbox/tb\\_camb\\_form.cfm](http://lambda.gsfc.nasa.gov/toolbox/tb_camb_form.cfm)

<sup>3</sup> <http://www.ccs.tsukuba.ac.jp/Astro/Members/ishiyama/greem>

<sup>4</sup> <http://code.google.com/p/phantom-grape/>

**Table 1.** Details of the  $\nu^2$ GC simulations.  $N$  is the total number of particles,  $L$  is the comoving box size,  $m$  is the particle mass,  $\varepsilon$  is the Plummer softening length, and  $M_{\min}$  is the mass of the smallest halos identified by the FoF algorithm with a linking length of  $b = 0.2$ . The number of particles for the smallest halos is 40. With the exception of the  $\nu^2$ GC-H3 simulation, which was terminated at  $z = 4$ , all other simulations were terminated at  $z = 0$ .

Name	$N$	$L(h^{-1}\text{Mpc})$	$m(h^{-1}M_{\odot})$	$\varepsilon(h^{-1}\text{kpc})$	$M_{\min}(h^{-1}M_{\odot})$
$\nu^2$ GC-L	$8192^3 = 549,755,813,888$	1120.0	$2.20 \times 10^8$	4.27	$8.79 \times 10^9$
$\nu^2$ GC-M	$4096^3 = 68,719,476,736$	560.0	$2.20 \times 10^8$	4.27	$8.79 \times 10^9$
$\nu^2$ GC-S	$2048^3 = 8,589,934,592$	280.0	$2.20 \times 10^8$	4.27	$8.79 \times 10^9$
$\nu^2$ GC-H1	$2048^3 = 8,589,934,592$	140.0	$2.75 \times 10^7$	2.14	$1.10 \times 10^9$
$\nu^2$ GC-H2	$2048^3 = 8,589,934,592$	70.0	$3.44 \times 10^6$	1.07	$1.37 \times 10^8$
$\nu^2$ GC-H3	$4096^3 = 68,719,476,736$	140.0	$3.44 \times 10^6$	1.07	$1.37 \times 10^8$

**Table 2.** Statistics of halos at  $z = 0$ . The total number of halos is listed in the second column.  $M_{\max}$  is the mass of the largest halo identified in each simulations.  $N_{\max}$  is the number of particles in the largest halos, and  $F_{\text{fof}}$  is the ratio between the total mass of all halos identified by the FoF algorithm and that of the simulation box.

Name	#Halos	$M_{\max}(h^{-1}M_{\odot})$	$N_{\max}$	$F_{\text{fof}}$
$\nu^2$ GC-L	421,801,565	$4.11 \times 10^{15}$	18,685,583	0.485
$\nu^2$ GC-M	52,701,925	$2.67 \times 10^{15}$	12,120,576	0.485
$\nu^2$ GC-S	6,575,486	$1.56 \times 10^{15}$	7,107,526	0.474
$\nu^2$ GC-H1	5,467,200	$4.81 \times 10^{14}$	17,476,256	0.526
$\nu^2$ GC-H2	4,600,746	$4.00 \times 10^{14}$	116,397,797	0.555

mass resolution comparable with those of the  $\nu^2$ GC-L simulation was reported by Heitmann et al. (2014). However, their simulation is still based on the WMAP7 cosmology (Komatsu et al. 2011), which is significantly different from the Planck cosmology adopted in this study.

Our  $\nu^2$ GC-L simulation offers the highest mass resolution among simulations utilizing boxes larger than  $1 h^{-1}\text{Gpc}$ . Compared with the Millennium simulation (Springel et al. 2005), the  $\nu^2$ GC-L simulation performed with 55 times more particles, four times better mass resolution, and 11 times larger volume. Because two times better mass resolution and three times larger volume are obtained with the  $\nu^2$ GC-H3 simulation, this simulation is better suited to studying galaxies at high redshifts than the Millennium-II simulation (Boylan-Kolchin et al. 2009), whose properties are comparable with those of the  $\nu^2$ GC-H1 and  $\nu^2$ GC-H2 simulations.

Note that outside the regions displayed in Figure 1, there are many large simulations adopting over  $2048^3$  particles, including Horizon Runs (Kim et al. 2009; Kim et al. 2011), MultiDark simulations (Prada et al. 2012), DEUS (Alimi et al. 2012), MICE series (Fosalba et al. 2008; Crocce et al. 2010; Fosalba et al. 2013), Jubilee (Watson et al. 2014), Dark Sky Simulations (Skillman et al. 2014), and the Outer Rim (Heitmann et al. 2014). Because adopting a larger box in these simulations resulted in poorer mass resolution, galaxy and AGN formation are not targets of these simulations (even in simulations with larger particles than the  $\nu^2$ GC-L (Skillman et al. 2014; Heitmann et al. 2014)). Conversely, there are some studies adopted smaller boxes and higher mass resolutions, including Ishiyama et al. (2009b), Cosmogrid (Portegies Zwart et al. 2010; Groen et al. 2011; Ishiyama et al. 2013; Rieder et al. 2013a; Rieder et al. 2013b), halos hosting the first stars at high redshifts (Sasaki et al. 2014),

the smallest halos first formed in the Universe (Ishiyama 2014), and  $N$ -body simulations of the Milky Way Galaxy (Bédorf et al. 2014). Such simulations are rare because the simulation timestep must be small, since the dynamical time scale is short relative to larger box simulations. If the same number of particles is used, simulations become less computationally challenging as the box size increases.

## 2.2. Halo Identification

We identified halos in each output redshift using the Friends-of-Friends (FoF) algorithm (Davis et al. 1985) with a linking parameter of  $b = 0.2$ . The number of particles for the smallest halo is 40. We list several halo properties across all simulations in Table 2: the number of halos, the mass and number of particles in the largest halos, and the ratio between the total mass of all halos and that of the simulation box. The number of halos of the largest run,  $\nu^2$ GC-L, is 421,801,565. For all simulations,  $\sim 50\%$  of dark matter exists inside halos.

The simplest definition of the halo mass is the sum of the masses of all member particles of an FoF group. Yet another way to define the halo mass is to sum the masses of the particles in a spherical region with average density larger than the cosmic critical density by a factor of an overdensity parameter. A frequently used overdensity parameter is 200 or some values according to the spherical collapse model (Bryan & Norman 1998). In our halo catalogs, both the FoF mass and the spherical mass with the overdensity parameter of Bryan & Norman (1998) are computed. Throughout this study, we use the FoF mass as the halo mass.

Figure 2 shows the images of the  $\nu^2$ GC-L simulation at  $z = 0$ . The largest halo of the  $\nu^2$ GC-L consists of 18,685,583 particles, and its mass is  $4.11 \times 10^{15} h^{-1}M_{\odot}$ . The bottom right panel of Figure 2 is a close-up image of



the largest halo. Figure 3 shows the redshift evolution of cosmic structures of the  $\nu^2$ GC-L,  $\nu^2$ GC-H1, and  $\nu^2$ GC-H2 simulations.

### 2.3. Merger Tree

From the halo catalogs, we generated merger trees of the six simulations. The algorithm to generate merger trees is as follows. If a halo at redshift  $z_i$  has the largest fraction of its number of particles in common with those of a halo at redshift  $z_{i-1}$  ( $z_i < z_{i-1}$ ), the halo at redshift  $z_i$  is assigned as the descendant of the halo at redshift  $z_{i-1}$ , making the halo at redshift  $z_{i-1}$  the progenitor of that at redshift  $z_i$ . A halo always has only one descendant, however, a descendant halo can have a number of progenitor halos. We used all particles belong to each FoF halo regardless of whether they are self-bounded. However, there are approaches to increase the robustness of merger trees by using only a subset of most bound particles or trajectories of halos (e.g., Okamoto & Habe 2000; Harker et al. 2006; Behroozi et al. 2013b).

The FoF algorithm can connect physically separated halos into a single halo. Such halos can easily fragment, emerge again at a later time, and remerge with the host halo. Typically, the mass of such halos is near the resolution limit. If we are not concerned with fragmentation, the number of mergers is overestimated. Since major mergers trigger many physical processes in the  $\nu^2$ GC model, the overestimation of mergers should be avoided. We can infer that a large fraction of baryonic gas in fragmented halos is lost and absorbed into the hot gas of host halos during the first mergers because baryonic gas acts in a collisional fashion, i.e., in a manner different from dark matter. We forcibly removed fragmented halos from merger trees after the first mergers. The same algorithm was also performed in the  $\nu$ GC merger trees (Nagashima et al. 2005). A similar algorithm was later called “stitch” by Fakhouri & Ma (2008). Several algorithms to remove fragmented halos have been proposed (e.g., Helly et al. 2003; Harker et al. 2006; Fakhouri & Ma 2008; Genel et al. 2009).

The algorithm to remove fragmented halos is as follows. If a progenitor (redshift  $z_{i-1}$ ) of a halo at redshift  $z_i$  is also the progenitor of smaller halos, the smaller halos are forcibly removed from the merger tree at redshift smaller than  $z_i$ . Sometimes, progenitors of fragmented halos are not found in FoF catalogs at redshift  $z_{i-1}$  and they fragment before redshift  $z_{i-2}$ . To handle such halos, we also search the progenitors at redshift  $z_{i-2}$ . If the progenitor is also the progenitor of larger halos at redshift  $z_i$ , the smaller halos is removed from the tree at redshift smaller than  $z_i$ . We performed this procedure up to redshift  $z_{i-4}$ . Differently from the “stitch” (Fakhouri & Ma 2008), the masses of smaller halos are not added on the mass of the larger halo in our algorithm. Therefore, halos can lose their masses when fragmentation of large halos occurs.

We define the most bounded particle in a halo as the marker particle of the halo. The spatial position of each halo (even in galaxies and AGNs) is determined by that of its marker particle.

In our merger trees, information about subhalos is not

included explicitly. Once halos fall into host halos and become subhalos, the properties of these halos after the merge, such as their masses, disappear in the merger tree. The evolution of subhalos in halos are modeled semi-analytically in the  $\nu^2$ GC model. The spatial positions of these subhalos are tracked using their marker particles assigned in time slices when they merge into their host halos.

In the evolution of halos, physical flybys occur frequently. At high redshift, flybys occur with similar frequency in mergers (Sinha & Holley-Bockelmann 2012). Close flybys can influence the evolution of halos and galaxies, although the effect is uncertain. Thus, flybys are not considered in current our merger trees.

## 3. Results

In this section, we present basic quantities describing halos in the  $\nu^2$ GC simulations, halo mass function, mass accretion rate, formation redshift, and merger statistics. We present updated fitting functions to describe these quantities as functions of the halo mass and redshifts. Compared with previously proposed fitting functions, we are able to use unprecedentedly large simulations with higher mass and spatial resolutions, and larger boxes (larger numbers of halos) in the state-of-the-art Planck cosmology. These differences may result in some differences in the basic quantities. We aim to not only extend the fitting functions for application to larger and smaller halo masses, but also provide the most advanced fitting functions for precise cosmology and accurate models of galaxy and AGN formation.

We exclude the  $\nu^2$ GC-H3 simulation from the following analysis, as it was terminated at  $z = 4$ . In some figures, the  $\nu^2$ GC-M and  $\nu^2$ GC-S simulations are excluded because many statistics of these simulations can not be distinguished from the largest simulation,  $\nu^2$ GC-L.

In §3.1, we use  $h^{-1}M_\odot$  as an unit of the halo mass. After §3.1, We alternatively use  $M_\odot$  to easily compare our results with previous studies.

### 3.1. Mass Function

In Figure 4, we plot the halo mass functions at  $z = 0$  for all  $\nu^2$ GC simulations except for the  $\nu^2$ GC-H3 simulation. The five mass functions are in good agreement with each other between the mass ranges of their resolutions (40 particles, dashed lines) and box size limits.

The halo mass functions are commonly described by

$$\frac{dn}{dM} = \frac{\rho_0}{M} \frac{d \ln \sigma^{-1}}{dM} f(\sigma), \quad (1)$$

where  $\rho_0$  is the mean mass density,  $\sigma$  is the mass variance, and  $f(\sigma)$  is an arbitrary fitting function. Several analytic functions (Press & Schechter 1974; Sheth et al. 2001) and empirical fitting functions have been proposed to fit well the results of cosmological simulations (e.g., Jenkins et al. 2001; Yahagi et al. 2004; Warren et al. 2006; Tinker et al. 2008; Angulo et al. 2012), and these are compiled in Murray et al. (2013). Here, we use a form described in

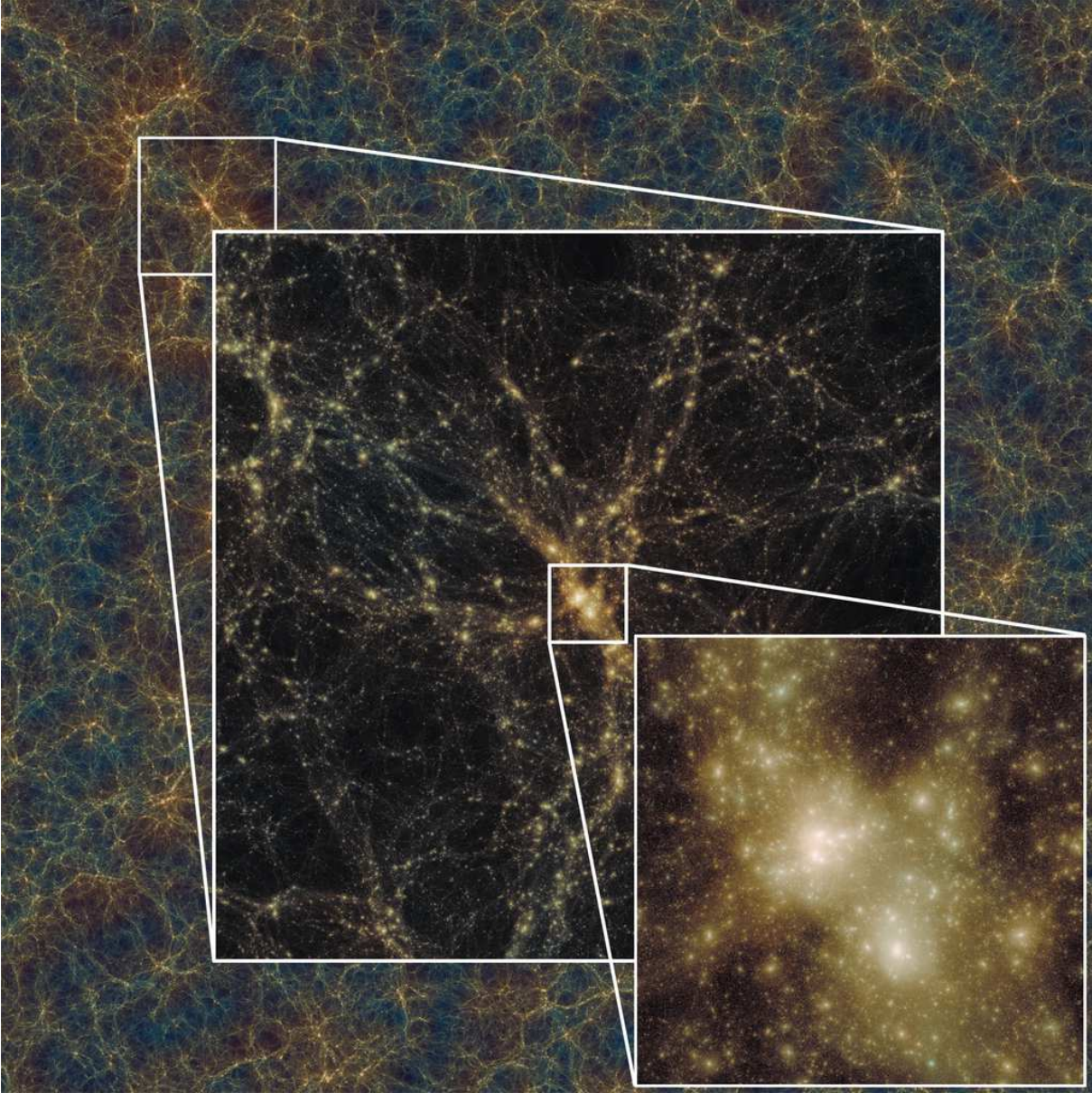


**Fig. 2.** Dark matter distribution in the largest  $\nu^2\text{GC-L}$  simulation at  $z=0$ . The background image shows a projected region with a thickness of  $45h^{-1}\text{Mpc}$  and a side length of  $1120h^{-1}\text{Mpc}$ . An enlargement of the largest halo is shown in the central image with a thickness of  $45h^{-1}\text{Mpc}$  and a side length of  $140h^{-1}\text{Mpc}$ . The bottom right panel is a close-up of the largest halo.



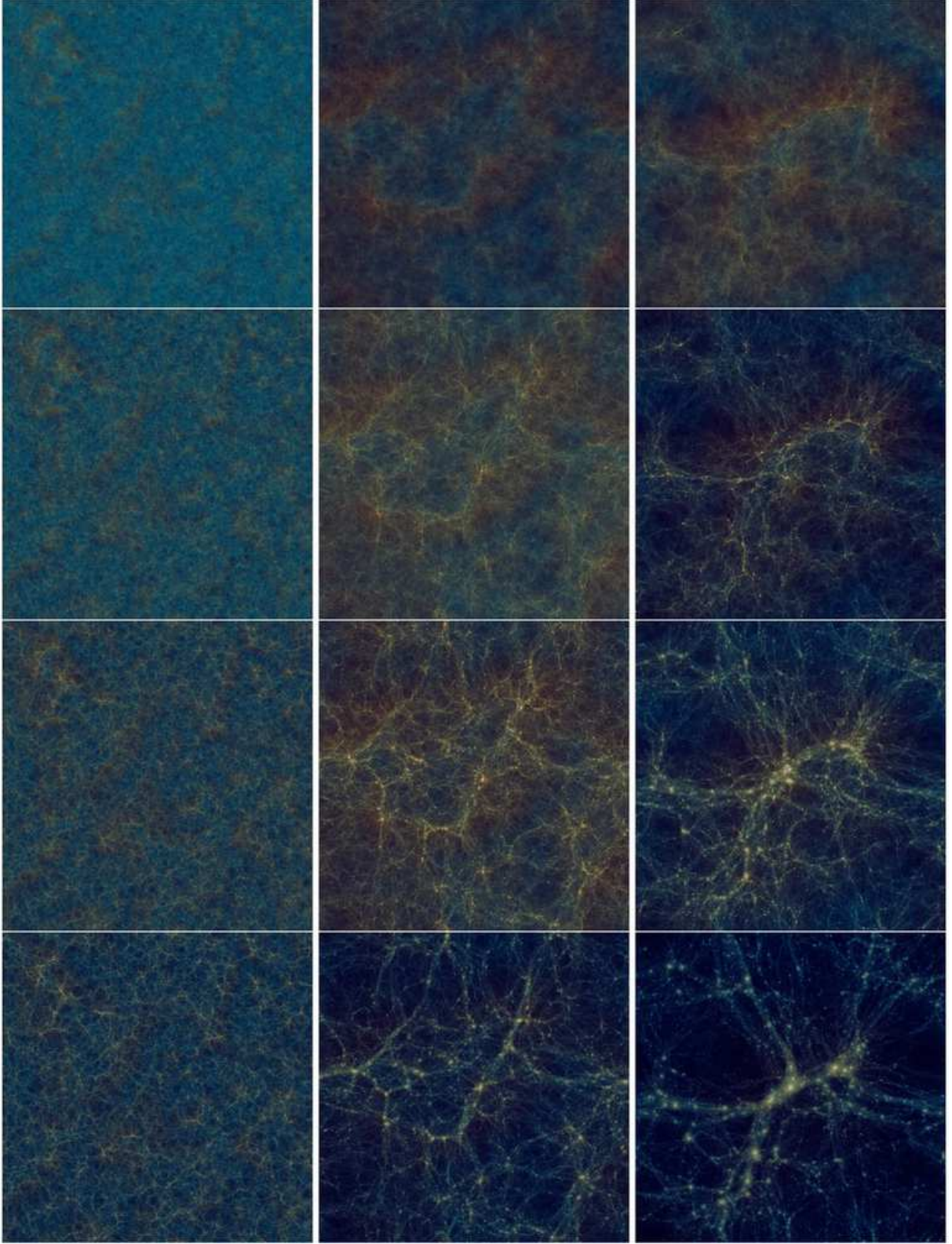


**Fig. 3.** Time evolution of cosmic structures of the  $\nu^2$ GC-L,  $\nu^2$ GC-H1, and  $\nu^2$ GC-H2 simulations (left to right). From top to bottom panels, epochs at  $z = 7.0$ ,  $3.0$ ,  $1.0$ , and  $0.0$  are shown. The thicknesses are  $45 h^{-1} \text{Mpc}$ ,  $42 h^{-1} \text{Mpc}$ , and  $21 h^{-1} \text{Mpc}$  for the  $\nu^2$ GC-L,  $\nu^2$ GC-H1, and  $\nu^2$ GC-H2 simulations, respectively. In the images of  $\nu^2$ GC-H1 and  $\nu^2$ GC-H2 simulations, the largest halos are in the center.

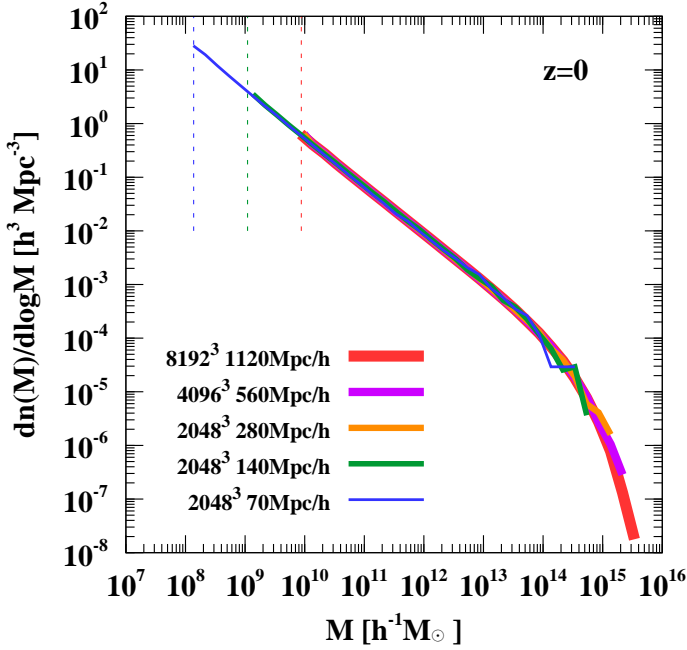


Fig. 4. Mass functions of dark matter halos in the  $\nu^2\text{GC}$  simulations. The vertical dashed bars show the minimum halo mass of each simulation (corresponding to 40 particles.)

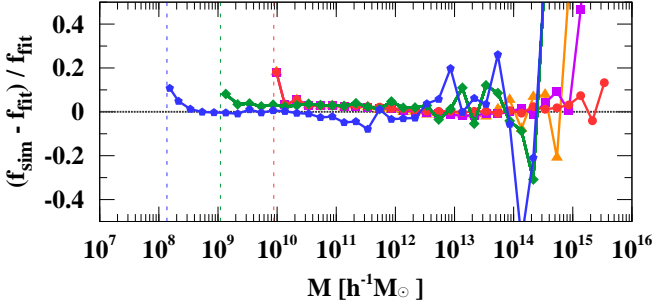


Fig. 5. Residuals of mass functions from the best fit function given by Equation (2). The style of each curve is the same as that in Figure 4. The vertical dashed bars show the minimum halo mass of each simulation (corresponding to 40 particles).

Warren et al. (2006),

$$f(\sigma) = A \left[ \left( \frac{B}{\sigma} \right)^C + 1 \right] \exp \left( -\frac{D}{\sigma^2} \right). \quad (2)$$

The best fit parameters to accurately describe the  $\nu^2\text{GC}$  simulations at  $z=0$  are  $A=0.193$ ,  $B=2.184$ ,  $C=1.550$ , and  $D=1.186$ .

Figure 5 shows the residuals of the mass functions from this best fit function. Evidently, this function fits all mass functions quite well for masses spanning nearly eight orders of magnitude. In most mass ranges, the accuracy is within 3%. The accuracy worsen at very high masses because of poor statistics and at very low masses because of the resolution effect.

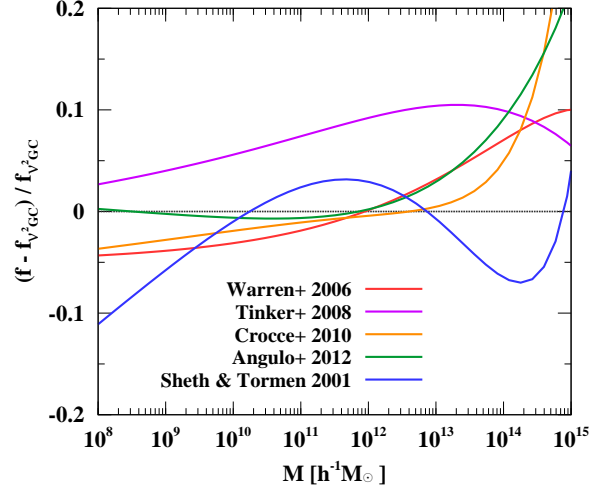


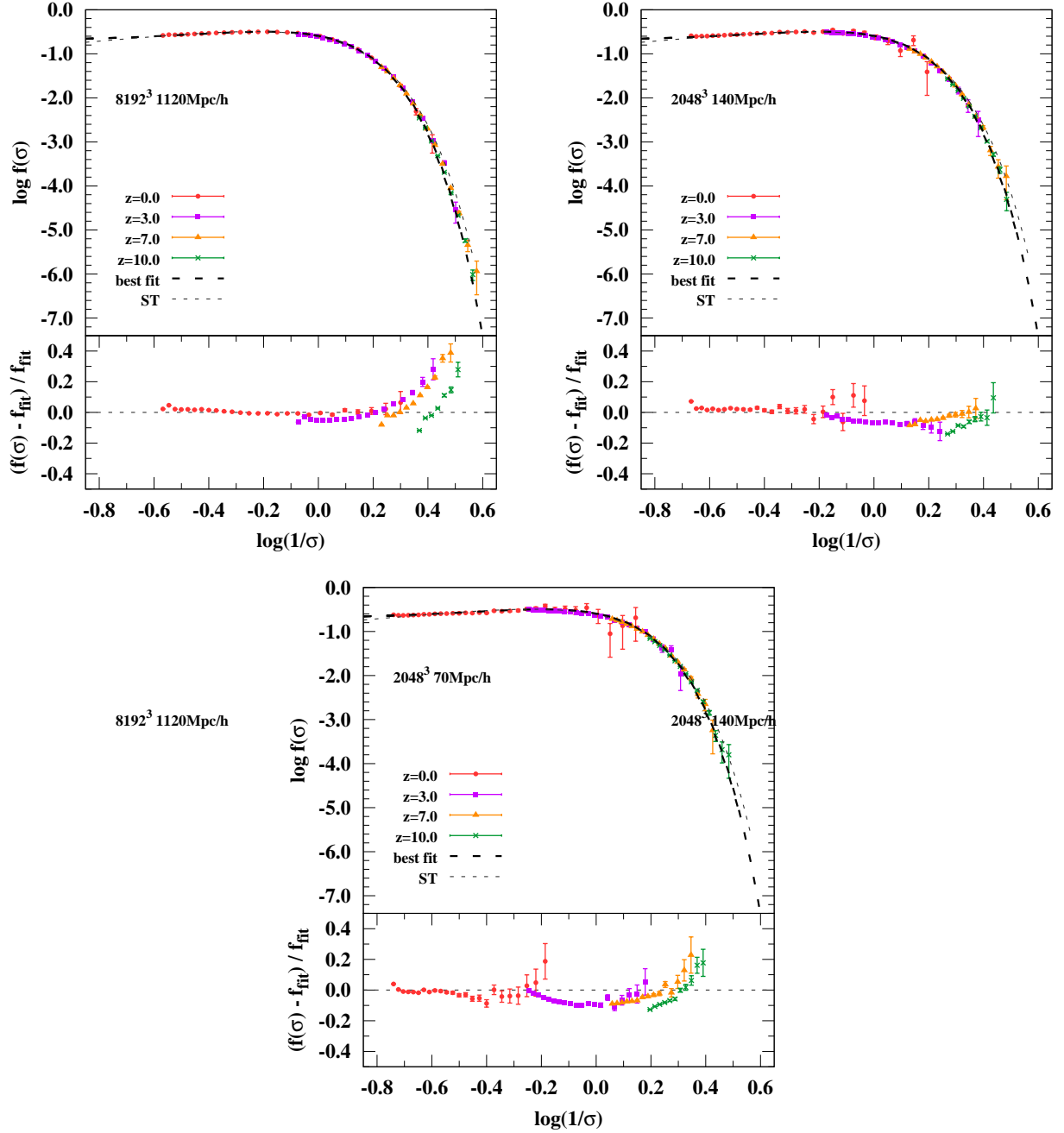
Fig. 6. Comparison of our best fit mass function with functions proposed by other studies for redshift  $z=0$ . (Sheth et al. 2001; Warren et al. 2006; Tinker et al. 2008; Crocce et al. 2010; Angulo et al. 2012).

The fitting form described in Equation (2) is the same as that used in Warren et al. (2006); Tinker et al. (2008); Crocce et al. (2010) and Angulo et al. (2012). In Table 3, we summarize the best fit parameters of these references. Figure 6 shows the residuals of these fitting functions and the function of Sheth et al. (2001) from our best fit function. All functions agree well within 10% in most mass ranges. For the mass larger than  $10^{14} h^{-1} M_{\odot}$ , the difference with Crocce et al. (2010) and Angulo et al. (2012) becomes larger. On the other hand, the agreement with the function of Angulo et al. (2012) is excellent for the mass smaller than  $10^{13} h^{-1} M_{\odot}$ . For the mass larger than  $10^{13} h^{-1} M_{\odot}$ , the functions of Sheth et al. (2001); Warren et al. (2006) and Tinker et al. (2008) are relatively close to our fit.

In the mass function of Equations (1) and (2), the dependence on the redshift and the cosmology is absorbed in the mass variance  $\sigma$ . It is worthwhile to verify that our best fit function can be applied to mass functions of different redshifts. In Figure 7, we plot the multiplicity functions of the  $\nu^2\text{GC-L}$ ,  $\nu^2\text{GC-H1}$ , and  $\nu^2\text{GC-H2}$  simulations for four different redshifts,  $z=0.0$ ,  $3.0$ ,  $7.0$ , and  $10.0$ . The multiplicity function reduces the dynamic range in the y-direction and helps us to understand the difference between mass functions. Clearly, from  $z=10$  to  $z=0$ , our best fit function could reproduce the mass functions of the simulations quite accurately over a wide range of masses. Since the multiplicity functions of the  $\nu^2\text{GC-M}$  and  $\nu^2\text{GC-S}$  simulations can not be distinguished from those of the  $\nu^2\text{GC-L}$  simulations, we did not include these functions in Figure 7 for visualization purposes.

The analytic function proposed by Sheth et al. (2001) is also plotted in Figure 7. The difference between this function and our best fit is negligible at  $z=0$ , but becomes larger as the redshift increases. Our fit yields slightly



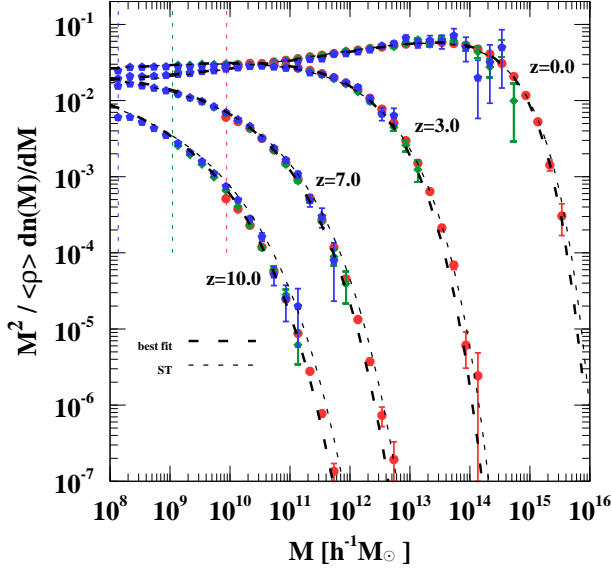


**Fig. 8.** Another look at multiplicity functions of the  $\nu^2$ GC-L,  $\nu^2$ GC-H1, and  $\nu^2$ GC-H2 simulations for four redshifts,  $z=0.0$ , 3.0, 7.0, and 10.0. In each panel, top figure is the mass variance  $\sigma$  versus  $f(\sigma)$  measured directly from the simulations, bottom figure shows residuals from the best fit. The colors of the symbols are the same as those used in Figure 4. The error bars show their Poisson error. The thick dashed line shows the best fit function. The thin dashed line represents the function of Sheth et al. (2001). For bottom figures, only data with errors less than 10% are shown.

$2048^3$  70 Mpc/h

**Table 3.** Best fit parameters of mass functions described in Equation (2) for redshift  $z = 0$ .

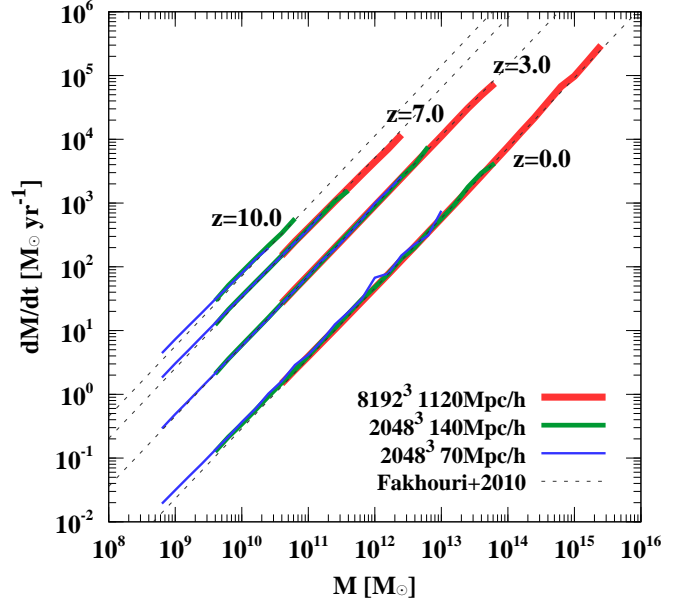
Reference	$A$	$B$	$C$	$D$
This work	0.193	2.184	1.550	1.186
Warren et al. (2006)	0.184	2.325	1.625	1.198
Tinker et al. (2008)	0.186	2.57	1.47	1.19
Crocce et al. (2010)	0.174	2.408	1.37	1.036
Angulo et al. (2012)	0.201	2.08	1.7	1.172

**Fig. 7.** Multiplicity functions of the  $\nu^2$ GC-L,  $\nu^2$ GC-H1, and  $\nu^2$ GC-H2 simulations for four redshifts,  $z = 0.0, 3.0, 7.0$ , and  $10.0$ . The colors of the symbols are the same as those used in Figure 4. The error bars show their Poisson error. The thick dashed line shows the best fit function given by Equation (2). The thin dashed line represents the function of Sheth et al. (2001).

smaller values than the previously proposed one though the difference is still negligible. The overprediction of the model by Sheth et al. (2001) at high redshifts is consistent with other simulations (e.g., Reed et al. 2007; Klypin et al. 2011; Watson et al. 2013).

Figure 8 gives another look at multiplicity functions, the mass variance  $\sigma$  versus  $f(\sigma)$  measured directly from the  $\nu^2$ GC-L,  $\nu^2$ GC-H1, and  $\nu^2$ GC-H2 simulations for four different redshifts  $z = 0.0, 3.0, 7.0$ , and  $10.0$ . Since our best fit function shows excellent agreement with the simulation results, excluding the high mass region because of poor statistics, we can say that this fit is at least universal with respect to the redshift.

In each panel of Figure 8, the residuals of  $f(\sigma)$  from the best fit are also shown. For most areas of  $-0.7 \leq \log(\sigma^{-1}) \leq 0.3$ , the accuracy is within 10%. Apparently, the accuracy becomes worse with increasing redshift for  $\log(\sigma^{-1})$  larger than 0.3, simply because our best fit is calibrated in the mass range of  $5 \times 10^8 \sim 3 \times 10^{15} h^{-1} M_\odot$  at  $z = 0$ , corresponding to  $-0.7 \leq \log(\sigma^{-1}) \leq 0.3$ . Special attention is needed to use our best fit beyond  $\log(\sigma^{-1})$  larger than 0.3, corresponding to  $\sim 3 \times 10^{11} h^{-1} M_\odot$  at  $z = 10$ .

**Fig. 9.** Mean mass accretion rate of the  $\nu^2$ GC-L,  $\nu^2$ GC-H1, and  $\nu^2$ GC-H2 simulations as a function of the halo mass for four redshifts,  $z = 0.0, 3.0, 7.0$ , and  $10.0$ . The dashed line is the relation proposed by Fakhouri et al. (2010) derived from the Millennium and Millennium-II simulations.

The fitting form described in Equation (2) is the same as that used in Warren et al. (2006); Tinker et al. (2008); Crocce et al. (2010) and Angulo et al. (2012), however, the best fit parameters are different, and their applicability to high redshifts was not confirmed. The  $\nu^2$ GC simulations are the first to extend this simple form to suit a wide range of redshifts.

### 3.2. Mass Accretion Rate

There are many studies for the mass accretion and assembly history (e.g., Wechsler et al. 2002; van den Bosch 2002; Li et al. 2007; Zhao et al. 2009; McBride et al. 2009; Fakhouri et al. 2010; Bosch et al. 2014; Correa et al. 2014; Correa et al. 2015). By tracking merger trees, we can derive the mass accretion history of each halo as follows. Given a halo with mass  $M_i$  at redshift  $z_i$  ( $i$  stands for redshift), we track its merger tree and identify  $M_{i-1,j}$ , the masses of its progenitors ( $M_{i-1,j} > M_{i-1,j+1}$ ,  $j$  denotes the rank of the progenitors) at redshift  $z_{i-1}$  ( $z_i < z_{i-1}$ ). The most massive progenitor is  $M_{i-1,0}$ . We then compute the mass accretion  $dM/dt = (M_i - M_{i-1,0})/dt$ , where  $dt$  is the time interval between snapshots at redshifts  $z_i$  and

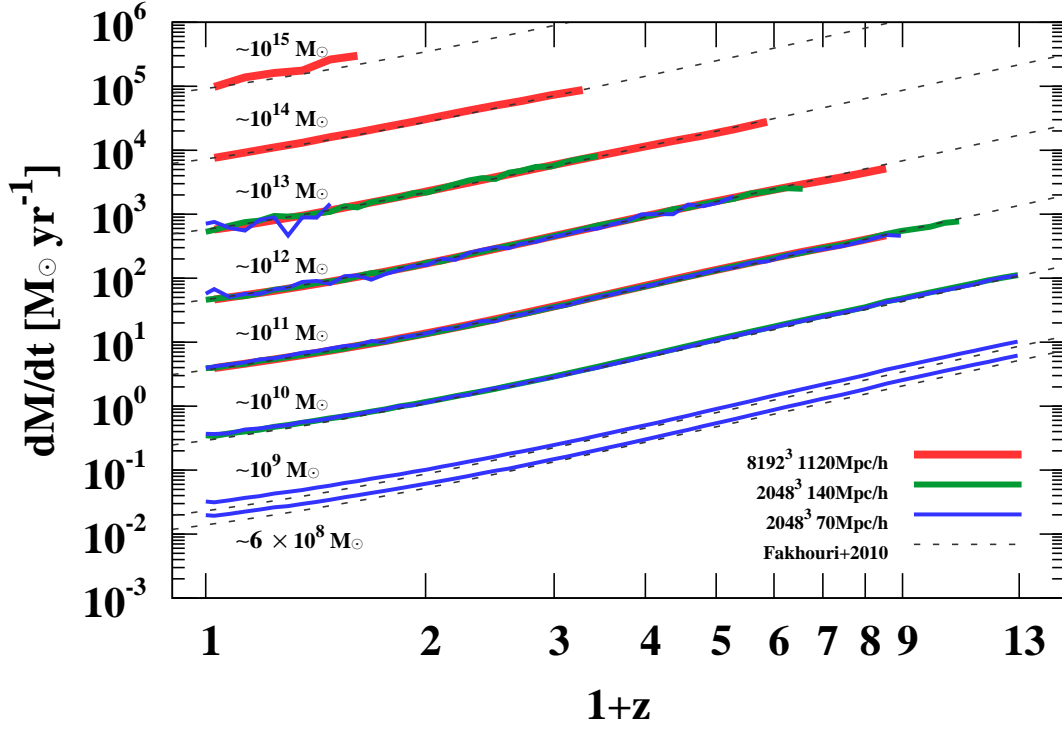


**Fig. 10.** Redshift evolution of mean mass accretion rate of the  $\nu^2$ GC-L,  $\nu^2$ GC-H1, and  $\nu^2$ GC-H2 simulations over halo masses of approximately seven orders of magnitude. The dashed line is the relation proposed by Fakhouri et al. (2010) derived from the Millennium and Millennium-II simulations.

$z_{i-1}$ .

Hereafter, we use  $M_\odot$  as an unit of the halo mass to easily compare our results with previous studies. Figure 9 shows the mean mass accretion rates of the  $\nu^2$ GC-L,  $\nu^2$ GC-H1, and  $\nu^2$ GC-H2 simulations as a function of the halo mass. We only plot mass bins larger than halos of 40 particles and containing minimum 100 halos. For  $z = 10$ , the mean mass accretion rate of  $\nu^2$ GC-L is not shown because the time interval between snapshots at high redshifts is not sufficiently small. The three results are in good agreement with each other, reinforcing the convergence of the  $\nu^2$ GC simulations. The dependence of the mass accretion rate on the halo mass is similar regardless of the redshift. We confirm that the fitting function suggested by Fakhouri et al. (2010) (the updated fitting function of McBride et al. (2009) based on the Millennium simulation) agrees well with our results (dashed line). This fitting function is given by (Fakhouri et al. 2010)

$$\left\langle \frac{dM}{dt} \right\rangle = 46.1 M_\odot \text{yr}^{-1} \left( \frac{M}{10^{12} M_\odot} \right)^{1.1} \times (1 + 1.11z) \sqrt{\Omega_0(1+z)^3 + \lambda_0}. \quad (3)$$

The dependence of the mass accretion rate per unit mass  $\frac{1}{M} \frac{dM}{dt}$  on the halo mass is weak ( $\propto M^{0.1}$ ), however, its dependence on the redshift is nearly  $\propto (1+z)^{1.5}$  at low redshifts and  $\propto (1+z)^{2.5}$  for  $z > 1$ .

We plot the redshift evolution of the mean mass accretion rate for the  $\nu^2$ GC-L,  $\nu^2$ GC-H1, and  $\nu^2$ GC-H2 simulations in Figure 10 over halo masses of approximately seven orders of magnitude. Only redshift bins containing

over 100 halos are plotted. As shown in Figure 9, the fitting function suggested by Fakhouri et al. (2010) can reproduce the dependence of the mass accretion rate on the halo mass and redshift fairly well. In Fakhouri et al. (2010), this dependence was confirmed in a relatively narrow mass range (from  $10^{10} M_\odot$  to  $10^{14} M_\odot$ ). We found that their fitting function is acceptable for the Planck cosmology, and we extended their results to a broader mass range (from  $\sim 6 \times 10^8 M_\odot$  to  $10^{15} M_\odot$ ) using the unprecedentedly high resolution and statistical power of the  $\nu^2$ GC simulations.

### 3.3. Halo Formation Redshift

Structure formation in the Universe proceeds hierarchically. Smaller halos collapse earlier than larger halos. We expect that a typical halo formation redshift  $z_f$  decreases monotonically as the halo mass increases. The extensive dataset of the  $\nu^2$ GC simulations allows us to quantify the halo formation redshift over a wide mass range with strong statistics to an extent that has not yet been achieved.

Typically, the halo formation redshift is defined as the redshift at which the most massive progenitor of the main branch of a halo reaches its half mass compared to  $z = 0$ . Fitting functions have been proposed using the Millennium simulations (e.g., McBride et al. 2009; Boylan-Kolchin et al. 2009). The halo formation redshift depends on the cosmological parameters. In this section, we update previous studies for the Planck Cosmology, and extend them to a wider range of masses using the  $\nu^2$ GC simulations.



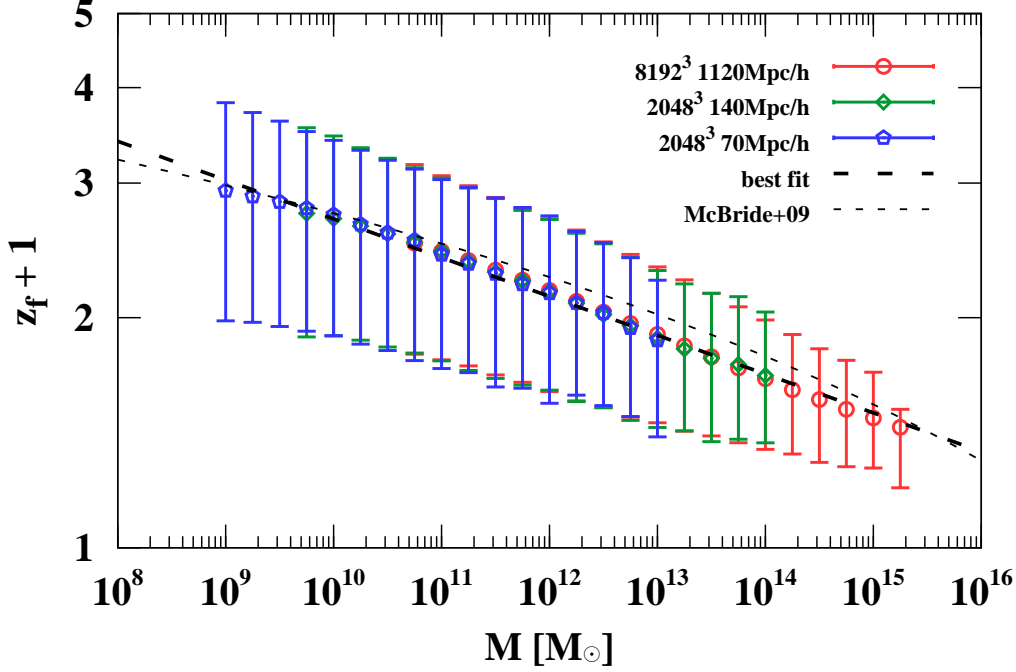


**Fig. 11.** Mean half mass formation redshift for the  $\nu^2$ GC-L,  $\nu^2$ GC-H1, and  $\nu^2$ GC-H2 simulations as a function of halo mass. The error bars show the 16% latest and earliest formation redshift. The thick dashed line is the best fit (Equation (4) in the text). Thin dashed line is a relation proposed by McBride et al. (2009) derived from the Millennium simulation.

Figure 11 shows the mean half mass formation redshift as a function of the halo mass for  $\nu^2$ GC-L,  $\nu^2$ GC-H1, and  $\nu^2$ GC-H2 simulations. The error bars show the 16% latest and earliest formation redshift. The three results agree well in the range larger than their resolution limits (over 150 particles). The best fit function is

$$1 + z_f = 2.69 \left( \frac{M}{10^{10} M_\odot} \right)^{-0.0508}. \quad (4)$$

In Figure 11, the fitting function obtained from the Millennium simulations (McBride et al. 2009) is plotted, and this function is consistent with the results but slightly overestimates the average formation redshift for masses greater than  $\sim 10^{10} M_\odot$ . The difference is  $\sim 11\%$  for Milky-Way-sized halos ( $\sim 10^{12} M_\odot$ ), although there are larger scatters.

What causes this difference? One possible cause is the difference of methods of extracting the merger trees. Another possibility is the difference in the adopted cosmological parameters. The cosmological parameters of the Millennium simulations are  $\Omega_0 = 0.25$ ,  $\Omega_b = 0.045$ ,  $\lambda_0 = 0.75$ ,  $h = 0.73$ ,  $n_s = 1$ , and  $\sigma_8 = 0.9$ , while those of the  $\nu^2$ GC simulations are based on the state-of-the-art Planck cosmology, namely,  $\Omega_0 = 0.31$ ,  $\Omega_b = 0.048$ ,  $\lambda_0 = 0.69$ ,  $h = 0.68$ ,  $n_s = 0.96$ , and  $\sigma_8 = 0.83$ . The striking differences between the Planck and Millennium cosmology are in parameters  $\Omega_0$ , and  $\sigma_8$ . Decreasing  $\Omega_0$  appears to decrease the average formation redshift. Conversely, increasing  $\sigma_8$  seems to increase the average formation red-

shift (e.g., van den Bosch 2002; Giocoli et al. 2012). Thus, the effect of the different cosmological parameters is not trivial, as seen in the internal structures of halos (Ludlow et al. 2014; Dutton & Macciò 2014).

To illustrate the cause of the difference of the mean half mass formation redshift between the results of the  $\nu^2$ GC and Millennium simulations, we performed a small additional simulation with the cosmology used in the Millennium simulations. The number of particles used was  $512^3$ , and the comoving box size was  $70 h^{-1} \text{Mpc}$ . The mass resolution was effectively equivalent with that adopted in the  $\nu^2$ GC-L,  $\nu^2$ GC-M, and  $\nu^2$ GC-S simulations. In Figure 12, we plot the average half mass formation redshifts of this simulation. Evidently, the results agree well with the fitting of McBride et al. (2009). This result suggests that the difference in simulation results is caused not by the implementation of extracting merger trees but by differences in cosmology.

### 3.4. Merger Rate

Given a halo with mass  $M_i$  at redshift  $z_i$  and its merger tree, we computed the merger mass ratio  $\xi = M_{i-1,j}/M_{i-1,0}$ , which is the ratio between the masses of the most massive progenitor and other progenitors. We then calculated the number of mergers per halo as a function of  $\xi$  and the descendant halo mass  $M_i$ . This definition of the mean merger rate is the same as that used in Fakhouri & Ma (2008) but is different from that discussed in Genel et al. (2009).

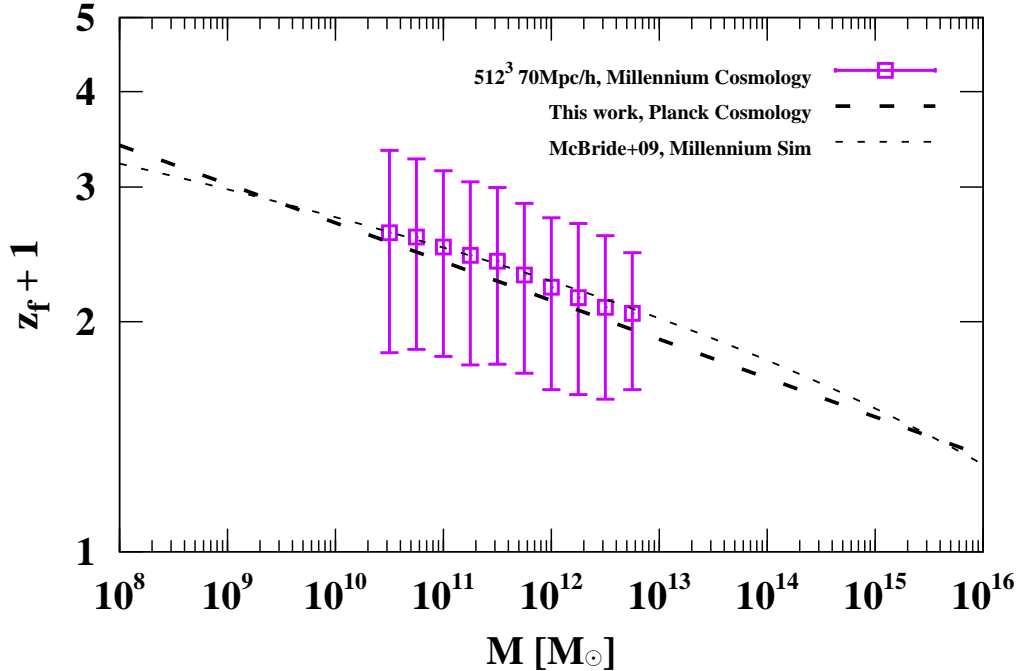


**Fig. 12.** Mean half mass formation redshift of an additional simulation adopting the same cosmology of the Millennium simulations. The error bars show the 16% latest and earliest formation redshift. The thick dashed line is the best fit derived from the  $\nu^2$ GC simulations based on the Planck cosmology (Equation (4) in the text). The thin dashed line is a relation proposed by McBride et al. (2009) derived from the Millennium simulation.

**Table 4.** Best fit parameters for the mean merger rate at  $z = 0$  as a function of the halo mass. The fitting function is given by Equation (5).

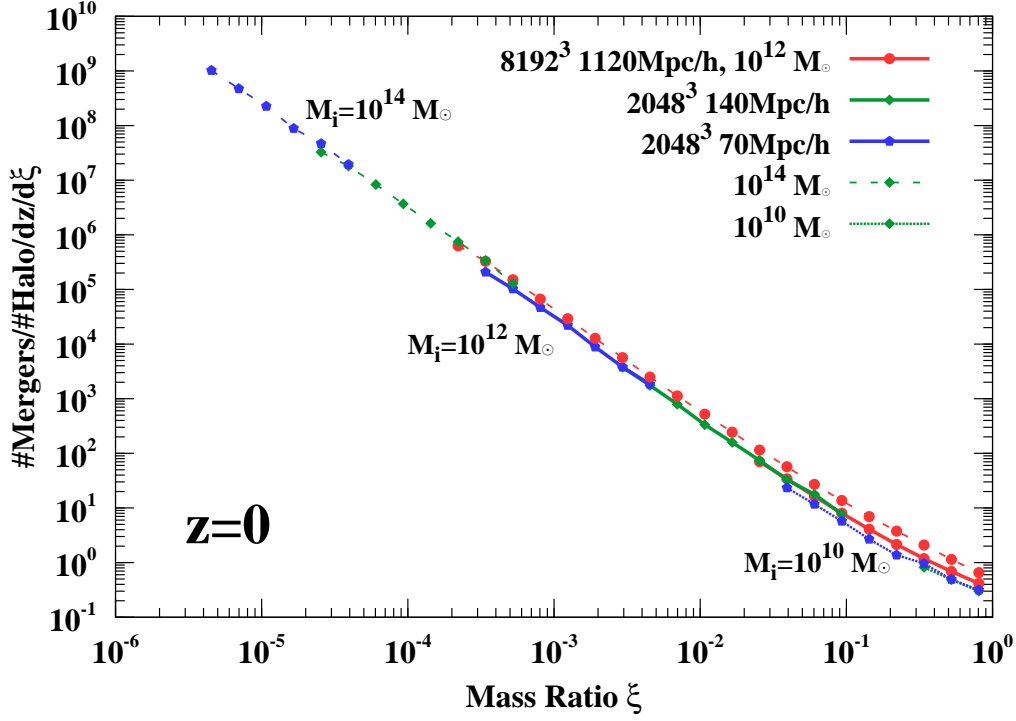
Mass range ( $M_\odot$ )	$A$	$\beta$	$\gamma$	$\xi_0$
$10^{15}-10^{15.25}$	0.0741	-1.917	0.549	0.0215
$10^{14}-10^{14.25}$	0.0792	-1.898	0.472	0.245
$10^{13}-10^{13.25}$	0.0715	-1.894	0.583	0.352
$10^{12}-10^{12.25}$	0.0357	-1.965	0.453	0.172
$10^{11}-10^{11.25}$	0.000788	-2.340	0.218	0.000308
$10^{10}-10^{10.25}$	0.00159	-2.360	0.290	0.00374

Figure 13 shows the number of mergers in the  $\nu^2$ GC-L,  $\nu^2$ GC-H1, and  $\nu^2$ GC-H2 simulations, per halo,  $dz$ , and  $d\xi$ , as a function of the merger mass ratio  $\xi$  at  $z = 0$  for three descendant mass bins,  $10^{10} M_\odot$ ,  $10^{12} M_\odot$ , and  $10^{14} M_\odot$ . We only plot  $\xi$  ranges in which  $\xi M_i$  is larger than the halos of 100 particles. In addition, we exclude  $\xi$  bins containing less than 80 mergers. For the mean merger rate at  $z = 0$ , we counted the number of mergers between  $z = 0.027$  and  $z = 0.078$ . The three simulations smoothly connect with each other although ranges with overlap are rather narrow. However, this configuration allows us to obtain the relation over a wide range of the merger mass ratios  $\xi$  from  $\sim 10^{-6}$  to unity.

In all mass ranges, the dependence of the mean merger rate on the mass ratio resembles a power law starting at the smallest mass ratio ( $\xi \sim 4 \times 10^{-6}$ ). The slope flattens as the mass ratio increases ( $\xi \geq 0.1$ ), which is consistent with results of previous studies (Fakhouri & Ma

2008; Genel et al. 2009; Fakhouri et al. 2010). The mean merger rate weakly depends on the halo mass such that halos with higher masses have larger numbers of mergers. Cluster-sized halos ( $\sim 10^{14} M_\odot$ ) experience  $\sim 1.5$  more mergers with high mass ratio ( $\xi > 0.33$ ) than Galaxy-sized halos ( $\sim 10^{12} M_\odot$ ).

The mass dependence is more striking in Figure 14, which shows the halo mass dependence of the integrated mean merger rate at  $z = 0$  for  $\xi \geq 0.33$ , 0.10,  $10^{-2}$ , and  $10^{-3}$ . Integrations were done from  $\xi$  to unity. The merger rate's weak dependence on the halo mass is qualitatively consistent with previous studies (Fakhouri & Ma 2008; dashed line). We confirm it over a wider mass range ( $10^9 M_\odot$  to  $10^{15} M_\odot$ ) because of the high resolution and powerful statistics of the  $\nu^2$ GC simulations. This qualitative agreement suggests that the mass dependence is weak and scales as  $\sim M^{0.08}$  (Fakhouri & Ma 2008). Indeed, the number of mergers with high mass ratio ( $\xi \geq 0.33$ ) of



**Fig. 13.** Mean merger rate of the  $\nu^2$ GC-L,  $\nu^2$ GC-H1, and  $\nu^2$ GC-H2 simulations as a function of merger mass ratio  $\xi$  at  $z=0$  for three descendant mass bins,  $M_i = 10^{10} M_\odot$  (dotted),  $10^{12} M_\odot$  (solid), and  $10^{14} M_\odot$  (dashed curves), respectively. The mean merger rate is defined as the number of mergers per halo,  $dz$ , and  $d\xi$ .

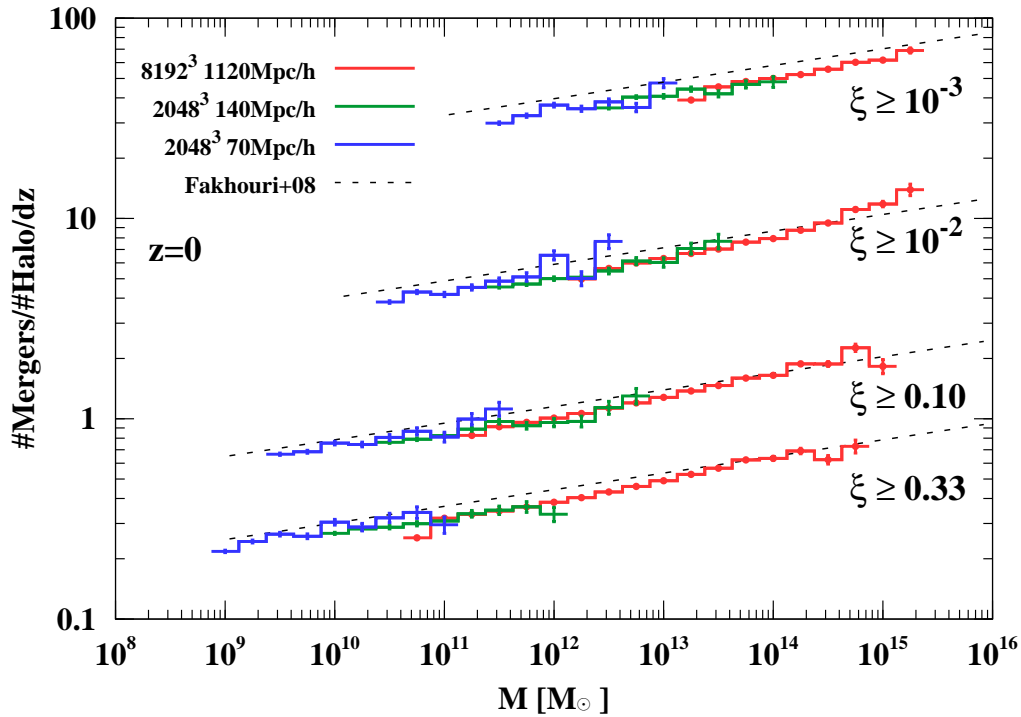


**Fig. 14.** Integrated mean merger rate and its Poisson error as a function of the halo mass at  $z=0$  for four  $\xi$  (merger mass ratio) bins,  $\xi = 0.33, 0.10, 10^{-2}$ , and  $10^{-3}$ , respectively. The dashed line is a fitting proposed by Fakhouri & Ma (2008) derived from the Millennium simulation.



$10^{14.5} M_\odot$  halos is  $\sim 2.4$  times larger than that of  $10^{10} M_\odot$  halos. Fakhouri et al. (2010) updated this fitting function using the Millennium-II simulation. Because the definition of the halo mass in their fitting function is different from that used in this study and Fakhouri & Ma (2008), we do not compare our results with Fakhouri et al. (2010).

As shown in Figure 14, the fitting function of Fakhouri & Ma (2008) slightly overpredicts the number of mergers, regardless of the merger mass ratio. To check the effect of different adopted cosmological parameters between the  $\nu^2$ GC and Millennium simulations, we performed an additional simulation with the cosmology used in the Millennium simulations. The number of particles used was  $1024^3$ , and the comoving box size was  $70 h^{-1} \text{Mpc}$ . The mass resolution was effectively equivalent with that adopted in the  $\nu^2$ GC-H1 simulation. In Figure 15, we plot the halo mass dependence of the integrated mean merger rate for this and  $\nu^2$ GC-H1 simulations. Clearly, the difference is tiny. This result implies that the difference in the mean merger rate might be caused by the implementation of extracting merger trees or the different mass resolutions.

We fit merger rates at  $z = 0$  in each mass bin into the following function,

$$\frac{1}{N_{\text{halo}}} \frac{dN_m}{d\xi dz} = A \xi^\beta \exp \left[ \left( \frac{\xi}{\xi_0} \right)^\gamma \right]. \quad (5)$$

Without terms depending on the halo mass and the redshift, this function is the same as that used in Fakhouri & Ma (2008) and Fakhouri et al. (2010). We searched best fit parameters to suit our simulation's results based on the Planck Universe. The best fit parameters are listed in Table 4. We found that best fit parameters show large scatters, implying that the merger rate can not be described accurately by a single universal function (see also Genel et al. 2009). Non-universality makes it difficult to obtain an accurate single fitting function for the mean merger rate.

The resolution of the time interval between the snapshots in the  $\nu^2$ GC simulations allow us to study the redshift evolution of the mean merger rate up to  $z \sim 6$  for the  $\nu^2$ GC-L simulation and up to  $z \sim 10$  for the  $\nu^2$ GC-H1 and  $\nu^2$ GC-H2 simulations. Figure 16 shows the redshift evolution of the integrated mean merger rate for three different mass bins ( $10^{12} M_\odot$ ,  $10^{13} M_\odot$ , and  $10^{15} M_\odot$ ) and five  $\xi$  bins ( $0.33$ ,  $0.03$ ,  $10^{-2}$ ,  $10^{-3}$ , and  $10^{-4}$ ). The three simulations agree well each other, reinforcing the convergence of the  $\nu^2$ GC simulations. The dependence on the redshift is negligible, which is consistent with previous studies (Fakhouri & Ma 2008; Fakhouri et al. 2010). Regardless of the redshift, a strong dependence on the merger rate and a weak mass dependence are always observed.

#### 4. Discussion and Summary

For deeper insights regarding galaxy and AGN formation, extremely large simulations with large volumes, large particle numbers, and high mass resolution to resolve small galaxies are required. We conducted six ul-

tralarge cosmological  $N$ -body simulations, which we called  $\nu^2$ GC simulations, on the basis of the concordance  $\Lambda$ CDM cosmology consistent with observational results obtained by the Planck satellite. The largest simulation consists of  $8192^3$  (550 billion) dark matter particles in a box of  $1.12 h^{-1} \text{Gpc}$  (a mass resolution of  $2.20 \times 10^8 h^{-1} M_\odot$ ). Among simulations utilizing boxes larger than  $1 h^{-1} \text{Gpc}$ , this is the highest resolution that has yet been achieved in a simulation.

In this study, we presented the numerical aspects and various properties of dark matter halos in the  $\nu^2$ GC simulation suite. Combining six large simulations, we can quantify the evolution of halos with masses of over eight orders of magnitude, from small dwarf galaxies to massive clusters. With the unprecedentedly high resolution and powerful statistics of the  $\nu^2$ GC simulations, we are able to study the halo mass function, mass accretion rate, formation redshift, and merger statistics. The results are summarized as follows.

1. We found that the halo mass function is well given by Equation (2), from  $10^8 M_\odot$  to  $10^{16} M_\odot$ , halo masses spanning nearly eight orders of magnitude, and from  $z = 10$  to  $z = 0$ . The analytic function of Sheth et al. (2001) slightly overpredicts the number of halos at high redshifts.
2. The halo mass accretion rate agrees well with the best fit function of Fakhouri et al. (2010) based on the Millennium simulations. We extended their results to a wider mass range (from  $\sim 6 \times 10^8 M_\odot$  to  $10^{15} M_\odot$ ) using the unprecedentedly high resolution and statistical power of the  $\nu^2$ GC simulations.
3. The half mass formation redshift is given by Equation (4). The fitting function obtained from the Millennium simulation (McBride et al. 2009) is consistent with our results, but slightly overestimates the formation redshift for masses greater than  $10^{10} M_\odot$ , probably owing to their different adopted cosmological parameters.
4. The fitting function of Fakhouri & Ma (2008) slightly overpredicts the number of mergers, though it qualitatively reproduces the weak dependence on the halo mass. The mean merger rate can not be described accurately by an universal function.

From the  $\nu^2$ GC simulations, we generated mock galaxy and AGN catalogs via our new semi-analytic galaxy formation model,  $\nu^2$ GC (Makiya et al., in prep), which is the successor of the  $\nu$ GC model (Nagashima et al. 2005). Our previous study combined a simulation comparable with the  $\nu^2$ GC-S simulation<sup>5</sup> and the  $\nu$ GC model, successfully reproduced the AGN downsizing trend (Enoki et al. 2014), and considered effects of dust attenuation on quasar luminosity functions (Shirakata et al. 2014). The combination of the unprecedentedly high resolution

<sup>5</sup> The number of particles used was  $2048^3$ , and the comoving box size was  $280 h^{-1} \text{Mpc}$ . This simulation is based on the WMAP7 (Komatsu et al. 2011), namely  $\Omega_0 = 0.2725$ ,  $\Omega_b = 0.0455$ ,  $\lambda_0 = 0.7275$ ,  $h = 0.702$ ,  $n_s = 0.961$ , and  $\sigma_8 = 0.807$ . The merger tree was extracted by the same way described in this paper.

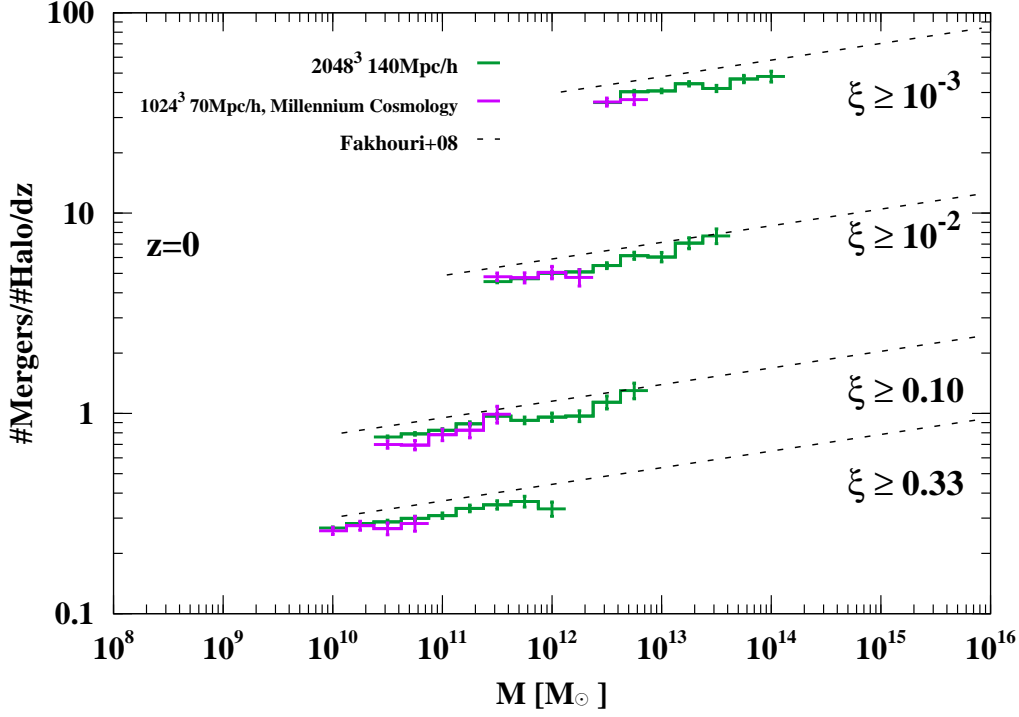


**Fig. 15.** Integrated mean merger rate and its Poisson error of an additional simulation adopting the same cosmology of the Millennium simulations at  $z=0$ , for four  $\xi$  (merger mass ratio) bins,  $\xi = 0.33, 0.10, 10^{-2}$ , and  $10^{-3}$ , respectively. The dashed line is a fitting proposed by Fakhouri & Ma (2008) derived from the Millennium simulation.

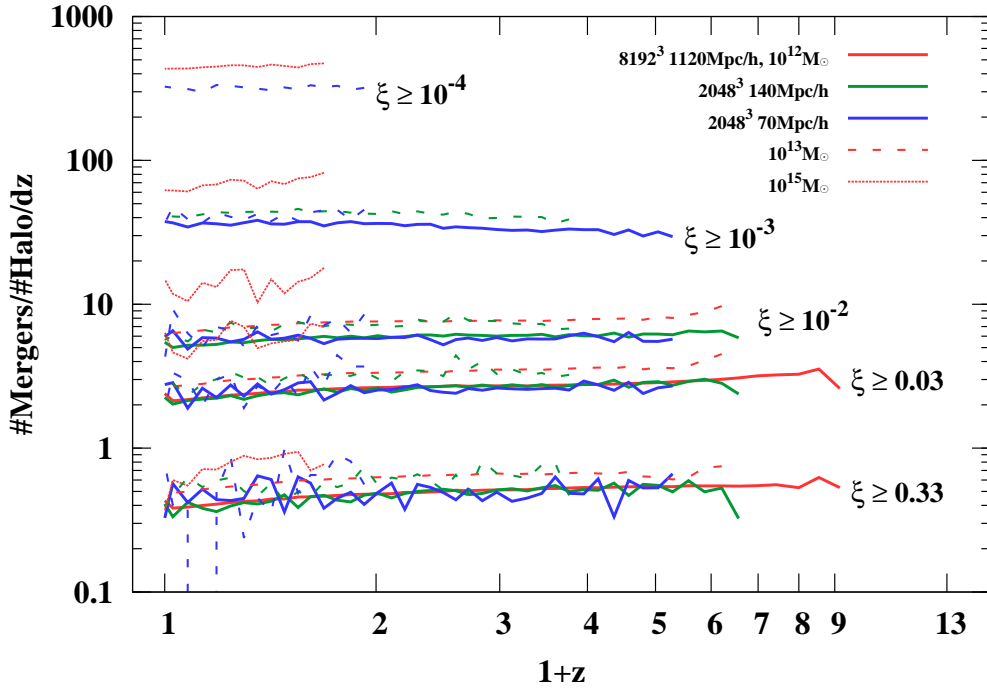


**Fig. 16.** Evolution of the integrated mean merger rate, for five  $\xi$  (merger mass ratio) bins,  $\xi = 0.33, 0.10, 10^{-2}, 10^{-3}$ , and  $10^{-4}$ , and for three descendant mass bins,  $M_i = 10^{12} M_\odot$  (solid),  $10^{13} M_\odot$  (dashed), and  $10^{15} M_\odot$  (dotted curves), respectively.

and powerful statistics of the  $\nu^2$ GC simulations and our new model opens a new window to study the formation and evolution of galaxies and AGNs from high to low redshifts. Together with Friends-of-Friends halo catalogs, the merger trees presented in this study, and halo and subhalo catalogs generated by the ROCKSTAR<sup>6</sup> phase space halo/subhalo finder (Behroozi et al. 2013a), we will make mock galaxy and AGN catalogs publicly available in the near future.

We thank the anonymous referee for his/her valuable comments. Numerical computations were partially carried out on Aterui supercomputer at Center for Computational Astrophysics, CfCA, of National Astronomical Observatory of Japan, and the K computer at the RIKEN Advanced Institute for Computational Science (Proposal numbers hp120286, hp130026, and hp140212). This study has been funded by Yamada Science Foundation, MEXT HPCI STRATEGIC PROGRAM, MEXT/JSPS KAKENHI Grant Numbers 24740115 and 25287041.

## References

- Alimi, J.-M., et al. 2012, in Proc. Int. Conf. High Performance Computing, Networking, Storage and Analysis, SC'12 (Los Alamitos, CA: IEEE Computer Society Press), 73:, (arXiv:1206.2838)
- Angulo, R. E., & Hilbert, S. 2014, arXiv: 1405.5888
- Angulo, R. E., Springel, V., White, S. D. M., Jenkins, A., Baugh, C. M., & Frenk, C. S. 2012, MNRAS, 426, 2046
- Angulo, R. E., & White, S. D. M. 2010, MNRAS, 405, 143
- Bédorf, J., Gaburov, E., Fujii, M. S., Nitadori, K., Ishiyama, T., & Zwart, S. P. 2014, in Proceedings of the International Conference for High Performance Computing, Networking, Storage and Analysis, SC '14 (Piscataway, NJ, USA: IEEE Press), 54–65, (arXiv:1412.0659)
- Behroozi, P. S., Wechsler, R. H., & Wu, H.-Y. 2013a, ApJ, 762, 109
- Behroozi, P. S., Wechsler, R. H., Wu, H.-Y., Busha, M. T., Klypin, A. A., & Primack, J. R. 2013b, ApJ, 763, 18
- Bond, J. R., Cole, S., Efstathiou, G., & Kaiser, N. 1991, ApJ, 379, 440
- Bosch, F. C. v. d., Jiang, F., Hearin, A., Campbell, D., Watson, D., & Padmanabhan, N. 2014, MNRAS, 445, 1713
- Bower, R. G. 1991, MNRAS, 248, 332
- Boylan-Kolchin, M., Springel, V., White, S. D. M., Jenkins, A., & Lemson, G. 2009, MNRAS, 398, 1150
- Bryan, G. L., & Norman, M. L. 1998, ApJ, 495, 80
- Correa, C. A., Wyithe, J. S. B., Schaye, J., & Duffy, A. R. 2014, arXiv: 1409.5228
- Correa, C. A., Wyithe, J. S. B., Schaye, J., & Duffy, A. R. 2015, arXiv: 1501.04382
- Crocce, M., Fosalba, P., Castander, F. J., & Gaztañaga, E. 2010, MNRAS, 403, 1353
- Crocce, M., Pueblas, S., & Scoccimarro, R. 2006, MNRAS, 373, 369
- Croom, S. M., et al. 2009, MNRAS, 399, 1755
- Davis, M., Efstathiou, G., Frenk, C. S., & White, S. D. M. 1985, ApJ, 292, 371
- Degraf, C., Di Matteo, T., & Springel, V. 2010, MNRAS, 402, 1927
- Dutton, A. A., & Macciò, A. V. 2014, MNRAS, 441, 3359
- Enoki, M., Ishiyama, T., Kobayashi, M. A. R., & Nagashima, M. 2014, ApJ, 794, 69
- Fakhouri, O., & Ma, C.-P. 2008, MNRAS, 386, 577
- Fakhouri, O., Ma, C.-P., & Boylan-Kolchin, M. 2010, MNRAS, 406, 2267
- Fontanot, F., Cristiani, S., Monaco, P., Nonino, M., Vanzella, E., Brandt, W. N., Grazian, A., & Mao, J. 2007, A&A, 461, 39
- Fosalba, P., Crocce, M., Gaztanaga, E., & Castander, F. J. 2013, arXiv: 1312.1707
- Fosalba, P., Gaztañaga, E., Castander, F. J., & Manera, M. 2008, MNRAS, 391, 435
- Genel, S., Genzel, R., Bouché, N., Naab, T., & Sternberg, A. 2009, ApJ, 701, 2002
- Giocoli, C., Tormen, G., & Sheth, R. K. 2012, MNRAS, 422, 185
- Groen, D., Portegies Zwart, S., Ishiyama, T., & Makino, J. 2011, Computational Science and Discovery, 4, 015001
- Guo, Q., White, S., Angulo, R. E., Henriques, B., Lemson, G., Boylan-Kolchin, M., Thomas, P., & Short, C. 2013, MNRAS, 428, 1351
- Harker, G., Cole, S., Helly, J., Frenk, C., & Jenkins, A. 2006, MNRAS, 367, 1039
- Heitmann, K., et al. 2014, arXiv: 1411.3396
- Helly, J. C., Cole, S., Frenk, C. S., Baugh, C. M., Benson, A., & Lacey, C. 2003, MNRAS, 338, 903
- Henriques, B., White, S., Thomas, P., Angulo, R., Guo, Q., Lemson, G., Springel, V., & Overzier, R. 2014, arXiv: 1410.0365
- Hirschmann, M., Dolag, K., Saro, A., Bachmann, L., Borgani, S., & Burkert, A. 2014, MNRAS, 442, 2304
- Ikeda, H., et al. 2011, ApJL, 728, L25
- Ikeda, H., et al. 2012, ApJ, 756, 160
- Ishiyama, T. 2014, ApJ, 788, 27
- Ishiyama, T., Fukushige, T., & Makino, J. 2009a, PASJ, 61, 1319
- Ishiyama, T., Fukushige, T., & Makino, J. 2009b, ApJ, 696, 2115
- Ishiyama, T., Nitadori, K., & Makino, J. 2012, in Proc. Int. Conf. High Performance Computing, Networking, Storage and Analysis, SC'12 (Los Alamitos, CA: IEEE Computer Society Press), 5:, (arXiv:1211.4406)
- Ishiyama, T., et al. 2013, ApJ, 767, 146
- Jenkins, A., Frenk, C. S., White, S. D. M., Colberg, J. M., Cole, S., Evrard, A. E., Couchman, H. M. P., & Yoshida, N. 2001, MNRAS, 321, 372
- Jiang, F., & van den Bosch, F. C. 2014, MNRAS, 440, 193
- Khandai, N., Di Matteo, T., Croft, R., Wilkins, S. M., Feng, Y., Tucker, E., DeGraf, C., & Liu, M.-S. 2014, arXiv: 1402.0888
- Kim, J., Park, C., Gott, J. R., & Dubinski, J. 2009, ApJ, 701, 1547
- Kim, J., Park, C., Rossi, G., Lee, S. M., & Gott, III, J. R. 2011, Journal of Korean Astronomical Society, 44, 217
- Klypin, A., Yepes, G., Gottlober, S., Prada, F., & Hess, S. 2014, arXiv: 1411.4001
- Klypin, A. A., Trujillo-Gomez, S., & Primack, J. 2011, ApJ, 740, 102
- Komatsu, E., et al. 2011, ApJS, 192, 18
- Lewis, A., Challinor, A., & Lasenby, A. 2000, ApJ, 538, 473

<sup>6</sup> <http://code.google.com/p/rockstar/>



- Li, Y., Mo, H. J., van den Bosch, F. C., & Lin, W. P. 2007, *MNRAS*, 379, 689
- Ludlow, A. D., Navarro, J. F., Angulo, R. E., Boylan-Kolchin, M., Springel, V., Frenk, C., & White, S. D. M. 2014, *MNRAS*, 441, 378
- Magorrian, J., et al. 1998, *AJ*, 115, 2285
- McBride, J., Fakhouri, O., & Ma, C.-P. 2009, *MNRAS*, 398, 1858
- Miyazaki, S., et al. 2006, in *Society of Photo-Optical Instrumentation Engineers (SPIE) Conference Series*, Vol. 6269, *Society of Photo-Optical Instrumentation Engineers (SPIE) Conference Series*
- Miyazaki, S., et al. 2012, in *Society of Photo-Optical Instrumentation Engineers (SPIE) Conference Series*, Vol. 8446, *Society of Photo-Optical Instrumentation Engineers (SPIE) Conference Series*, 0
- Murray, S. G., Power, C., & Robotham, A. S. G. 2013, *Astronomy and Computing*, 3, 23
- Nagashima, M., Yahagi, H., Enoki, M., Yoshii, Y., & Gouda, N. 2005, *ApJ*, 634, 26
- Nagashima, M., & Yoshii, Y. 2004, *ApJ*, 610, 23
- Nitadori, K., Makino, J., & Hut, P. 2006, *New A*, 12, 169
- Okamoto, T., & Habe, A. 2000, *PASJ*, 52, 457
- Peacock, J. A., & Heavens, A. F. 1990, *MNRAS*, 243, 133
- Planck Collaboration et al. 2014, *A&A*, 571, A16
- Portegies Zwart, S., et al. 2010, *IEEE Computer*, 43, 63
- Prada, F., Klypin, A. A., Cuesta, A. J., Betancort-Rijo, J. E., & Primack, J. 2012, *MNRAS*, 423, 3018
- Press, W. H., & Schechter, P. 1974, *ApJ*, 187, 425
- Reed, D. S., Bower, R., Frenk, C. S., Jenkins, A., & Theuns, T. 2007, *MNRAS*, 374, 2
- Rieder, S., Ishiyama, T., Langelaan, P., Makino, J., McMillan, S. L. W., & Portegies Zwart, S. 2013a, *MNRAS*, 436, 3695
- Rieder, S., van de Weygaert, R., Cautun, M., Beygu, B., & Portegies Zwart, S. 2013b, *MNRAS*, 435, 222
- Sasaki, M., Clark, P. C., Springel, V., Klessen, R. S., & Glover, S. C. O. 2014, *MNRAS*, 442, 1942
- Sheth, R. K., Mo, H. J., & Tormen, G. 2001, *MNRAS*, 323, 1
- Shirakata, H., Okamoto, T., Enoki, M., Nagashima, M., Kobayashi, M. A. R., Ishiyama, T., & Makiya, R. 2014, *arXiv: 1412.1478*
- Sinha, M., & Holley-Bockelmann, K. 2012, *ApJ*, 751, 17
- Skillman, S. W., Warren, M. S., Turk, M. J., Wechsler, R. H., Holz, D. E., & Sutter, P. M. 2014, *arXiv: 1407.2600*
- Spergel, D. N., et al. 2003, *ApJS*, 148, 175
- Springel, V., et al. 2005, *Nature*, 435, 629
- Tanikawa, A., Yoshikawa, K., Nitadori, K., & Okamoto, T. 2013, *New A*, 19, 74
- Tanikawa, A., Yoshikawa, K., Okamoto, T., & Nitadori, K. 2012, *New A*, 17, 82
- Teyssier, R., et al. 2009, *A&A*, 497, 335
- Tinker, J., Kravtsov, A. V., Klypin, A., Abazajian, K., Warren, M., Yepes, G., Gottlöber, S., & Holz, D. E. 2008, *ApJ*, 688, 709
- van den Bosch, F. C. 2002, *MNRAS*, 331, 98
- Warren, M. S., Abazajian, K., Holz, D. E., & Teodoro, L. 2006, *ApJ*, 646, 881
- Watson, W. A., Iliev, I. T., D'Aloisio, A., Knebe, A., Shapiro, P. R., & Yepes, G. 2013, *MNRAS*, 433, 1230
- Watson, W. A., Iliev, I. T., Diego, J. M., Gottlöber, S., Knebe, A., Martínez-González, E., & Yepes, G. 2014, *MNRAS*, 437, 3776
- Wechsler, R. H., Bullock, J. S., Primack, J. R., Kravtsov, A. V., & Dekel, A. 2002, *ApJ*, 568, 52
- White, M., Cohn, J. D., & Smit, R. 2010, *MNRAS*, 408, 1818
- Yahagi, H., Nagashima, M., & Yoshii, Y. 2004, *ApJ*, 605, 709
- Zhao, D. H., Jing, Y. P., Mo, H. J., & Börner, G. 2009, *ApJ*, 707, 354